Journal of Power Sources, 49 (1994) 333–348

Three-dimensional and time-dependent simulation of a planar solid oxide fuel cell stack

E. Achenbach
Research Centre Jülich, Energy Process Engineering Institute, 52425 Jülich (Germany)

Abstract

The mathematical simulation of a planar solid oxide fuel cell (SOFC) is presented. The model accounts for three-dimensional and time-dependent effects. Internal methane-steam reforming and recycling of the anode gas are also considered. The effects of different flow manifolding, i.e., cross-, co-, or counter-flow are discussed. After a short description of the mathematical procedure, computational results are presented. In particular the distribution of the gases, of the current density and of the solid structure temperature across the cell are shown. Furthermore the effects of different flow manifolding, of radiation from the outer stack surface to the surroundings and of anode gas recycling on the operating conditions of the stack are considered. The response of the cell voltage to a load change is also discussed.

Introduction

Mathematical modelling is an important tool for the design of solid oxide fuel cells (SOFC) and for the prediction of their normal and transient operating conditions. Some work has been done in this field with increasing interest during the last two years. Based on the first computations by Vayenas and Hegedus [1], the detailing degree of the mathematical modelling has increased [2–15] so that at the present time the following requirements can be formulated.

It has become evident that internal reforming of methane is a crucial point to be considered since the cooling effect of the endothermal reforming reaction strongly affects the operating conditions of the cell stack.

It has been shown that the heat transferred by the surface of the stack to the surroundings influences the temperature field significantly so that a three-dimensional simulation becomes compulsory to account for these effects.

The steam necessary for the reforming reaction can be advantageously taken from the fuel cell system itself. Since double the amount of H_2O is electrochemically produced than is needed for the reforming process, partial feedback of the anode gas is recommended to minimize engineering expenses. Therefore the simulation should include recycling of the anode gas.

It is important to know about the response of the complete fuel cell stack to transient operating conditions. These occur during heating-up, cooling-down and load changes. The corresponding computational results yield time constants for the control of the system or may point out operating conditions which lead to failure of the plant.

To meet all these requirements a computer program has been developed characterized by the following specifications:

SSDI 0378-7753(93)01833-4

- three-dimensional and time-dependent simulation
- planar configuration in cross-, co- or counter-flow
- flexibility with respect to the geometry of the fuel and air channels including a frame containing the gas manifolding
- arbitrary inlet gas composition of CH_4, H_2O, H_2, CO, CO_2
- simultaneous electrochemical conversion of H_2 and CO applying the corresponding kinetics at the electrodes
- temperature-dependent ohmic resistances of the electrolyte, electrodes, bipolar plate and contact areas
- heat transfer by conduction, convection and radiation
- internal methane-steam reforming
- CO–CO_2 shift reaction at equilibrium
- feedback of the anode gas
- heat transfer by convection and radiation from the particular stack surfaces to the surroundings

The aim of the present paper is to point out the fundamentals of the mathematical model and to give some examples of the computational results. More detailed information is found in ref. 15.

Basic equations

The operation principle of the SOFC is sketched in Fig. 1. The electrochemically active region consists of the tri-layer represented by the cathode, electrolyte and anode. The electrodes — the cathode and the anode — are electron-conducting. The solid electrolyte consisting of yttria stabilized zirconia dioxide is ion-conducting at high temperature transferring the charge by O^{2-} ions via the interstitials of the zirconia lattice. The oxidant is the oxygen from the air, the fuel is H_2 and CO produced by external or internal steam reforming of methane (CH_4).

The following chemical reactions are assumed to be relevant for an SOFC operated with air and methane as fuel.
Electrochemical reactions:

$$O_2 + 4e^- \longrightarrow O^{2-} + O^{2-} \text{ cathode} \tag{1}$$

$$H_2 + O^{2-} \longrightarrow H_2O + 2e^- \text{ anode} \tag{2}$$

$$CO + O^{2-} \longrightarrow CO_2 + 2e^- \text{ anode} \tag{3}$$

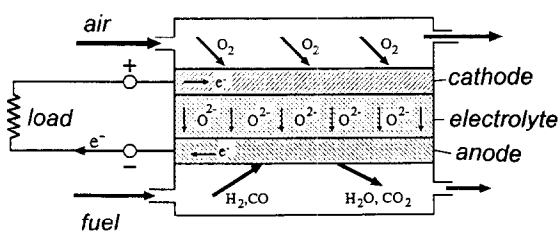

Fig. 1. Sketch of a planar SOFC.

Equations (1), (2) and (3) result in the following reactions:

$$H_2O + 0.5O_2 + 2e^- \longrightarrow H_2O + 2e^-$$

$$CO + 0.5O_2 + 2e^- \longrightarrow CO_2 + 2e^- \tag{4}$$

Steam reforming reaction:

$$CH_4 + H_2O \longrightarrow 3H_2 + CO \tag{5}$$

Shift reaction:

$$CO + H_2O \longrightarrow CO_2 + H_2 \tag{6}$$

It is assumed that the decomposition of methane according to:

$$CH_4 \longrightarrow 2H_2 + C \tag{7}$$

and the Boudouard reaction:

$$2CO \longrightarrow C + CO_2 \tag{8}$$

both forming carbon can be suppressed by selecting suitable wall materials and by providing a molar ratio of water to methane larger than two.

Except for the shift reaction eqn. (6) which is assumed to be always at equilibrium the electrochemical reactions eqns. (1)–(3) and the reforming reaction eqn. (5) are kinetically controlled. Some experimental kinetic data [16–22] are available for the cathode while those for the anode are very scarce [23, 24]. Due to the lack of better knowledge the overpotentials of the cathode and anode are calculated in this work from the following equations written in terms of electrical resistances:

Cathode

$$\frac{1}{R_c} = \frac{4F}{RT} k_c \left(\frac{p_{O_2}}{p^0}\right)^m \exp\left(-\frac{E_c}{RT}\right) \tag{9}$$

Anode H_2 conversion

$$\frac{1}{R_{A\,H_2}} = \frac{2F}{RT} k_{A\,H_2} \left(\frac{p_{H_2}}{p^0}\right)^m \exp\left(-\frac{E_A}{RT}\right) \tag{10}$$

Anode CO conversion

$$\frac{1}{R_{A\,CO}} = \frac{2F}{RT} k_{A\,CO} \left(\frac{p_{CO}}{p^0}\right)^m \exp\left(-\frac{E_A}{RT}\right) \tag{11}$$

The influence of the partial pressure on the overpotentials is accounted for by a slope of $m = 0.25$. The activation energy is set independent of the overpotential for both the cathode ($E_c = 160$ kJ mol^{-1}) and the anode ($E_A = 110$ kJ mol^{-1}) which may be admissible for low overpotentials. The data mentioned above are mean values from the cited literature. The pre-exponential factors are re-calculated values from experimental data. For the cathode it results from the assumption that the polarization resistance is: $R_c = 0.1\ \Omega\ cm^2$ at 1000 °C and $p_{O_2} = 0.21$ bar [20]. Similarly the pre-exponential factors of the H_2 and CO conversion are obtained. For this computation their values are: $k_c = 1.49 \times 10^{10}$; $k_{A\,H_2} = 2.13 \times 10^8$; $k_{A\,CO} = 2.98 \times 10^8$ A m^{-2}. The evaluation of the data is based on assumptions and therefore they cannot be considered as reliable experimental results.

The kinetics of the reforming reaction are taken from our own yet unpublished experiments at a nickel cermet. It was seen that the reaction order of the CH_4 partial pressure is unity and that the vapor partial pressure has no catalytic effect on the reaction. Therefore the results of the conversion rate of CH_4 can be expressed by the following equation:

$$\dot{r}_{CH_4} = k_{CH_4} p_{CH_4} \exp(-E_{CH_4}/RT) \tag{12}$$

The activation energy has a value of $E_{CH_4} = 82$ kJ/mol and the pre-exponential factor is $k_{CH_4} = 4274$ (mol m^{-2} $bars^{-1}$ s^{-1}).

The equilibrium constant of the shift reaction is determined by:

$$k_{shift} = \exp(-\Delta G/RT) \tag{13}$$

The open-circuit potential (OCP) in the cell is a local quantity, as it depends on the actual gas composition at the cathode and anode. It can be determined by the Nernst equation:

$$U^0 = U^\infty - (RT/2F) \ln(p_{H_2O}/(p_{H_2} p_{O_2}^{1/2})) \tag{14}$$

Equation (14) holds for hydrogen. Since the shift reaction is assumed to be at equilibrium, the OCP of CO is equal to that of H_2.

If an electrical current is passed through the cell the voltage reduces on account of its internal resistances. These are due to the overpotentials at the cathode and anode, the ohmic losses of the tri-layer and those of the bipolar plate. Equations (15) and (16) yield the relationship between the actual cell voltage and the local current density assuming that the total current passes the cathode and the ohmic resistances and that the anodic current divides according to the particular H_2 or CO conversion.

$$U = U_{H_2}{}^0 - (R_{OHM} j + R_{H_2} j_{H_2} + R_C j) \tag{15}$$

$$U = U_{CO}{}^0 - (R_{OHM} j + R_{CO} j_{CO} + R_C j) \tag{16}$$

In addition following equation must be satisfied for the anode current density:

$$j = j_{H_2} + j_{CO} \tag{17}$$

The mass balance for the fuel channel was made with respect to CH_4, H_2, H_2O, CO and CO_2, that for the air channel to O_2. The conversion rates of the particular gas components result from eqns. (9)–(13) taking into account the stoichiometric factors from eqns. (1)–(6). For example the mass balance of H_2 yields for the volume element:

$$\partial \dot{n}''_{H_2}/\partial x = 3\dot{r}_{CH_4}/h_f + \Delta \dot{n}'_{SHIFT} - \dot{r}_{el\,H_2}/h_f \tag{18}$$

A corresponding sets of equations must be provided for the remaining gas components.

The energy balances have to be done separately for the fuel flow, the air flow and the solid structure. For this rise it is assumed, that all reaction enthalpies are released at the tri-layer system and that, therefore, the reaction enthalpies occur in the source term of the solid structure balance.

The balance of the gas flow accounts for the heat transferred from the channel walls to the gas and for the heat capacity of the gases with respect to their composition. Thus we obtain:

Fuel

$$\partial(\dot{n}'' c_p T)_f/\partial x = [\alpha_f (T_s - T_f) + (\dot{n} c_p)_{prod} T_s - (\dot{n} c_p)_{ed} T_f]/h_f \tag{19}$$

Air

$$\partial(\dot{n}'' c_p T)_a/\partial x = [\alpha_a(T_s - T_a) - (\dot{r} c_p)_{elO_2}]/h_a \tag{20}$$

Solid

$$\rho_s c_{ps} \frac{\partial T_s}{\partial t} = \lambda_{ef,x} \frac{\partial^2 T_S}{\partial x^2} + \lambda_{ef,y} \frac{\partial^2 T_S}{\partial y^2} \lambda_{ef,z} \frac{\partial^2 T_S}{\partial z^2} + \Phi \tag{21}$$

The solid is considered to be a quasi-homogeneous material with respect to heat conductivity. An effective conductivity is then defined separately for each coordinate accounting for the conduction through the solid and gas phase, and by means of radiation as well. The source term, Φ, contains the sum of the reaction enthalpies as mentioned above and the convective heat rates minus the electrical energy. The boundary conditions of eqn. (21) are kept flexible and allow for heat convection and radiation from each of the stack surfaces to a wall of arbitrary temperature.

The computation proceeds as follows. In addition to all geometry and property data, the mean current density, the degree of pre-reforming, the air ratio and the fuel utilization are given quantities from which the molar flux of the fuel and air are determined. The temperature of the solid structure is then set to an initial temperature, say 900 °C. Now the mass balance is made associated with the energy balance of the gas flow side to obtain the source terms for the energy balance of the solid structure. After this, eqn. (21) can be solved together with its boundary conditions. When the local convergence is achieved the calculation proceeds with a time increment of Δt. The computation is terminated when the results of two succeeding time steps differ less than a prescribed threshold ϵ.

For two-dimensional calculations the top and bottom areas of the cell are treated as being adiabatic. For the three-dimensional case the results of the two-dimensional computation serve as the initial values of the whole stack. Then the energy balance is made for the solid structure to account for the effect imposed by the outer boundary conditions.

Since the stack is treated as a homogeneous body the spatial increments in the tri-layer plane must not coincide with the stack sub-geometry. In the direction normal to this plane, however, Δz is equal to the height of a single cell.

Results

Reference cell

To point out the effect of particular parameters on the operating conditions of a stack a reference case is defined. It consists of an adiabatic cell, 130 mm × 130 mm in size, ten fuel and ten air channels in cross-flow, 100 mm × 100 mm electrochemically active area surrounded by a frame of 15 mm width containing the gas manifolds. The fuel is a gas mixture of CH_4, H_2, H_2O, CO_2 and CO. Its composition results from a mixture of $H_2O/CH_4 = 2.5$ after 30% pre-reforming at CO shift equilibrium. A certain degree of pre-reforming is recognized to be necessary when natural gas is applied which contains a low amount of higher hydrocarbons. Those hydrocarbons are prone to decomposition at high temperatures which results in carbon formation. The gas inlet temperature is 900 °C, the total pressure 1 bar and the fuel utilization $U_f = 85\%$. The air ratio $\lambda = 7$ is chosen so that the temperature increase on the air side is about 100 °C along the cell. Finally the mean current density is $j = 300$ mA cm^{-2}.

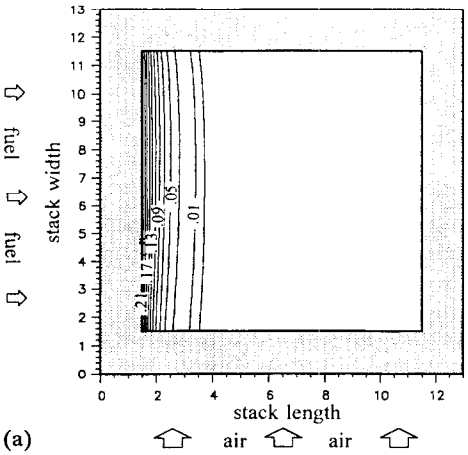

(a)

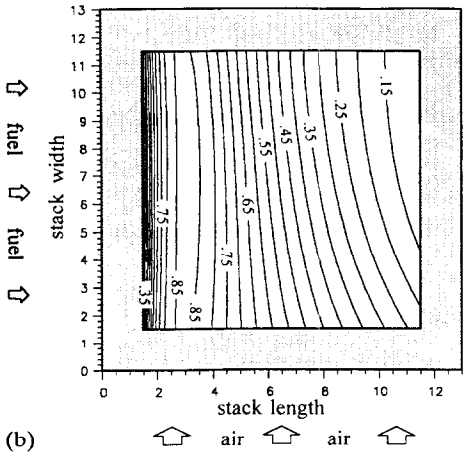

(b)

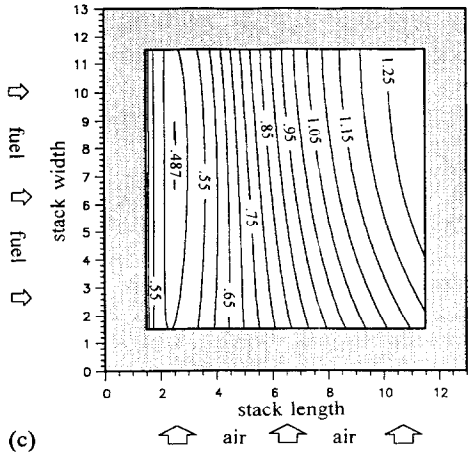

(c)

Fig. 2. *(continued)*

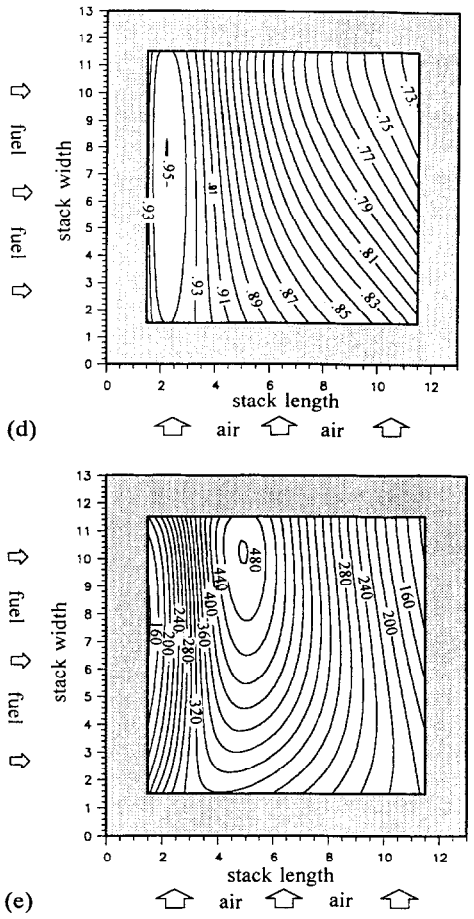

Fig. 2. Local quantities of the reference cell: molar distribution of (a) CH_4; (b) H_2; (c) H_2O; (d) open-circuit potential, and (e) current density.

Figure 2(a)–(e) shows some characteristic results of the reference cell. Due to the very fast reforming reaction methane is completely converted in the first 15 mm of the cell (Fig. 2(a)). Therefore the hydrogen partial pressure increases (Fig. 2(b)) while water is consumed in this area (Fig. 2(c)). This leads to a high OCP (Fig. 2(d)). The temperature breaks down due to the strong endothermal reforming reaction (Fig. 3(a)) which is the reason that the current density maximum (Fig. 2(e)) does not occur at the location of maximum Nernst potential, but somewhat further downstream. The CO distribution is rather similar to that of H_2 as a consequence of shift equilibrium. Downstream of the H_2 maximum the educts, i.e. H_2 and CO are gradually converted by means of the electrochemical reactions to H_2O and CO_2. The depletion of O_2 at the cathode is of minor importance because a high stoichiometry air ratio of $\lambda = 7$ is necessary to cool down the cell under the conditions mentioned above.

Table 1 gives additional computational results of the gas composition, the molar fluxes and mean gas temperatures for the reference cell. The cell voltage corresponding to the mean current density of 300 mA cm^{-2} is $U = 0.682$ V which results in an

TABLE 1

Gas composition and temperatures of the reference cell

	Inlet	Outlet
Flow rate fuel, n_f (mol h^{-1})	0.674	0.903
Flow rate air, n_a (mol h^{-1})	10.97	10.64
Gas composition		
H_2 (%)	26.26	7.85
CH_4 (%)	17.10	0.00
H_2O (%)	49.34	73.92
CO (%)	2.94	2.58
CO_2 (%)	4.36	15.65
Mean air temperature (K)	1173	1276
Mean fuel temperature (K)	1173	1260

electrical total power of $P_{el} = 20.46$ W. Referring P_{el} to the lower heating value of the pre-reformed inlet gas mixture an efficiency of $\eta_{n,in} = 52.2\%$ is obtained. $\eta_{\Delta n} = 63.3\%$ on the basis of the converted fuel and $\eta_{CH_4} = 55.8$ related to the methane input rate.

Effect of flow direction

From the engineering point of view the cross-flow of fuel and air in the cell is easiest to verify by the manifolding system. Therefore the cross-flow design is most frequently applied in the tests and theoretically considerations. Figures 3(b) and 3(c) show a comparison of the solid temperature distribution for counter- and co-flow with that of cross-flow (Fig. 3(a)). Since for cross-flow the temperature breaks down at the fuel entrance caused by the endothermal reforming reaction, the temperature drop is not so dramatic as for the co-flow (Fig. 3(c)) since the cooling air which has a temperature of about 900 °C supplies the reforming reaction with heat. The best situation is found for counter-flow because the air has the highest temperature at that location where the heat of the reforming reaction is required. Therefore the mean cell temperature is highest and the internal ohmic resistances lowest. This results in a better efficiency compared with cross- and co-flow (see Table 2).

Table 2 gives additional information about maximum temperature gradients occurring in the solid materials and about the non-uniformity of the current density distribution. Cross-flow yields the highest temperature gradients, which occur in the region of steam reforming. Co-flow is favorable with respect to the smallest variation of current density across the cell, since the distribution is symmetrical to the length axis of the cell — which is not the case for cross-flow — and since the solid temperature at the location of H_2 partial pressure maximum is lower compared with counter-flow.

Three-dimensional effects

The parameter studies show that the outer boundary conditions prevailing for a real cell stack have an important influence on the operation of the cell. At stack surface temperatures of $T_0 = 1000$ °C the equivalent heat transfer coefficient of the radiant heat transfer is $\alpha_r = 470$ W m^{-2} K^{-1}. This means that, if there is a temperature difference of only 10 °C between the stack surface and the vessel wall, about 5 kW m^{-2} are radiated from the stack. This demonstrates that an extremely effective thermal insulation of the vessels must be provided to protect the stack from cooling-out.

As an example Figs. 4(a) and 4(b) show the heat-loss effect on the temperature distribution in a stack radiating heat from the top plate only to the surroundings at 900 °C. Figure 4(a) refers to a stack of 50 cells under reference conditions and Fig. 4(b) to a stack under the same conditions but with metallic bipolar plates. It is evident that the heat losses affect the top region of the stack. The penetration depth is about five cells for the ceramic design (heat conductivity $\lambda_h = 2$ W m^{-1} K^{-1}) and nearly the whole stack height for the metallic plates ($\lambda_h = 27$ W m^{-1} K^{-1}). The radiated heat rate is 7% for the ceramic and 22% for the metallic stack with respect to the total amount of waste heat.

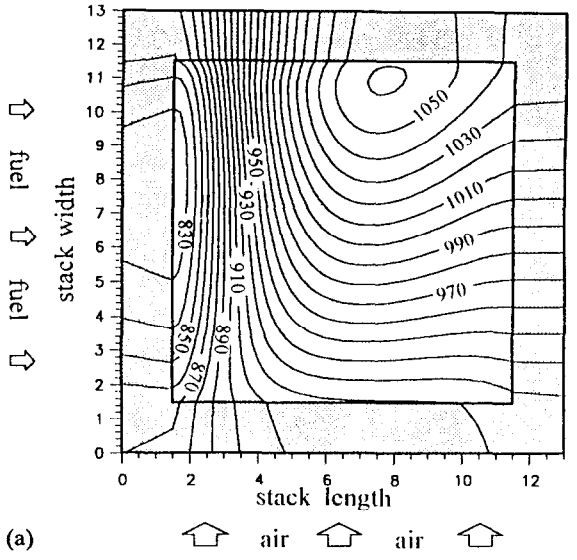

(a)

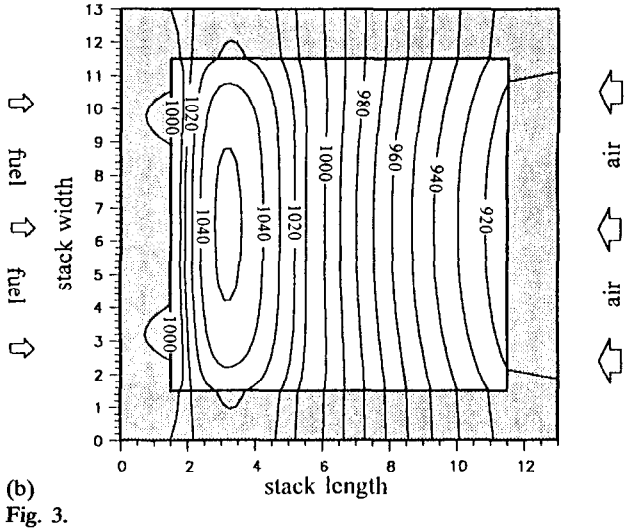

(b)

Fig. 3. *(continued)*

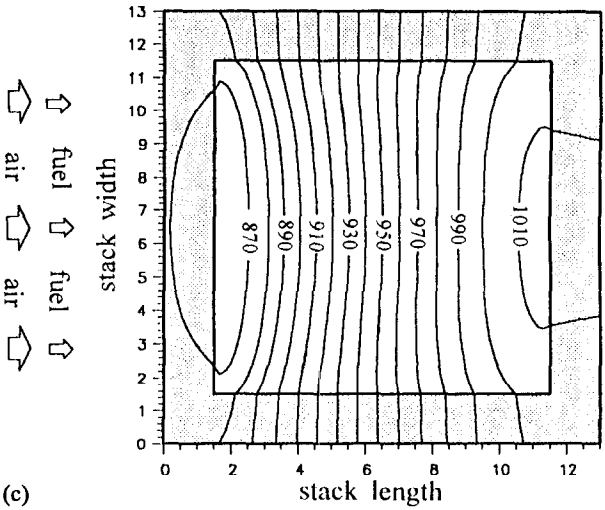

(c)

Fig. 3. Temperature of the solid structure for: (a) cross-flow; (b) counter-flow, and (c) co-flow.

TABLE 2

Performance data of cells in cross-, co- and counter-flow

	U (V)	P (W)	$\eta_{nf,in}$ (%)	$\theta_{s\,max}$ (°C)	$\theta_{s\,min}$ (°C)	$\theta_{a\,out}$ (°C)	$d\theta/ds_{max}$ (°C mm^{-1})	Δj_{max} (mA cm^{-2})
Cross-flow	0.682	20.46	52.2	1061	823	1003	7.09	368
Co-flow	0.674	20.21	51.6	1013	861	1008	5.08	184
Counter-flow	0.708	21.23	54.2	1052	910	1009	5.13	432

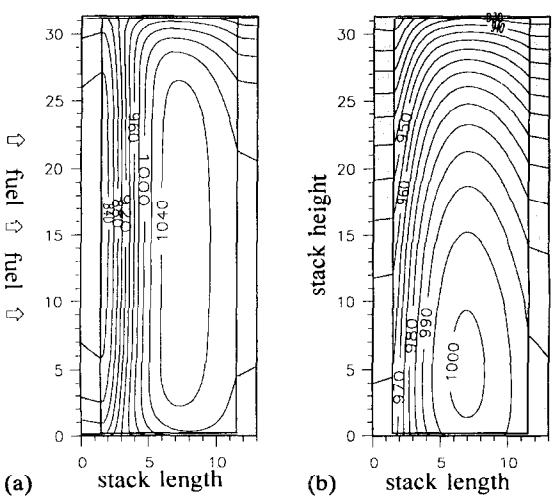

(a) (b)

Fig. 4. Solid temperature of a 50-cell stack with (a) ceramic, and (b) metallic bipolar plates.

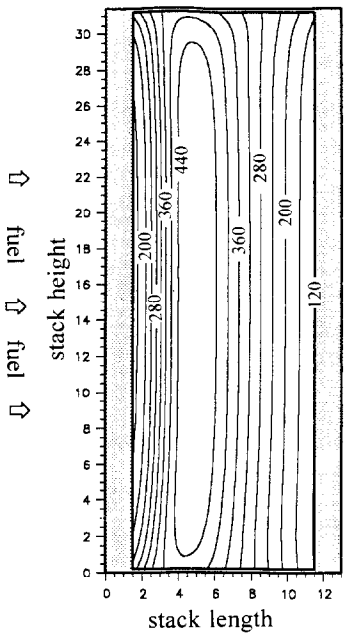

Fig. 5. Current density distribution in a ceramic stack.

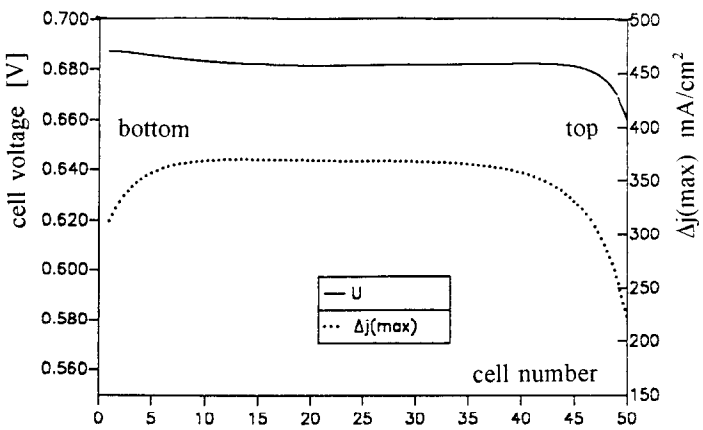

Fig. 6. Cell voltage and spread of current density along the stack height.

There are two consequences caused by the temperature decrease at the top of the stack. First, the internal resistance of the cells increases due to the increase of the ohmic losses in the electrolyte and of the overpotentials at the electrodes. Second, the lines of constant current density are no longer parallel to the vertical component (see Fig. 5) which means that the current passes the bipolar plates with a horizontal component. This results, due to longer current paths, in higher ohmic losses and finally in lower cell voltages. Figure 6 demonstrates this effect for a ceramic stack where cell no. 0 means the bottom and no. 50 the top cell from which the heat is radiated.

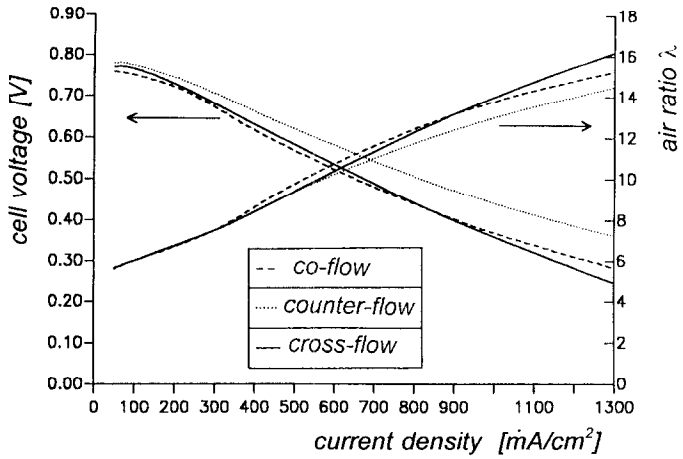

Fig. 7. Cell characteristics and air ratio under conditions of air temperature increase of $\Delta T = 100$ K.

Cell characteristics

The *U–j* cell characteristic has been computed for the reference cell under conditions of cross-, co-, and counter-flow (Fig. 7). The fuel utilization was kept constant at $U_f = 85\%$ while the air rate was varied such that the temperature increase of the cooling air was equal to $\Delta T = 100$ K. Since with increasing current density the heat losses increase, the air ratio has to be enhanced, too, to satisfy the above conditions. At a current density of 1000 mA/cm^2, for instance, an air ratio of $\lambda = 14$ is necessary to cool down the cell. This is, however, not acceptable for the case of once-through cooling with respect to the pumping power and to the expenses of the air heater. Therefore cathode gas recycling must be provided.

Furthermore, Fig. 7 demonstrates that counter-flow shows the best characteristics, for reasons already discussed above.

At low current density the curves flatten out whereas an increase in the value of the open-circuit potential (OCP) is expected. The reason for this is that the fuel utilization was kept constant along the cell characteristic. This means a decrease of mass flow with decreasing current density and therefore a local depletion of the fuel with an OCP near the actual cell voltage.

Load change

When the cell experiences a load change it will respond with a temperature variation. Since most of the physical and chemical processes involved are strongly temperature dependent, a transient behavior of the cell voltage is expected. Figure 8(a) exhibits the dynamic response of the cell voltage during load changes. Three cases have been considered assuming an instantaneous jump to a current density of $j = 500$ mA cm^{-2}. The starting levels are 200, 300 or 400 mA cm^{-2}. The Figure shows that an overshooting of the cell voltage occurs and that within 400 s steady-state conditions are reached again, independent of the jump height. The magnitude of the overshooting, however, increases with increasing jump height. The course of the cell voltage is closely related to the temperature of the solid material (Fig. 8(b)). The steady state of the cell voltage stabilizes when the stack temperatures have reached

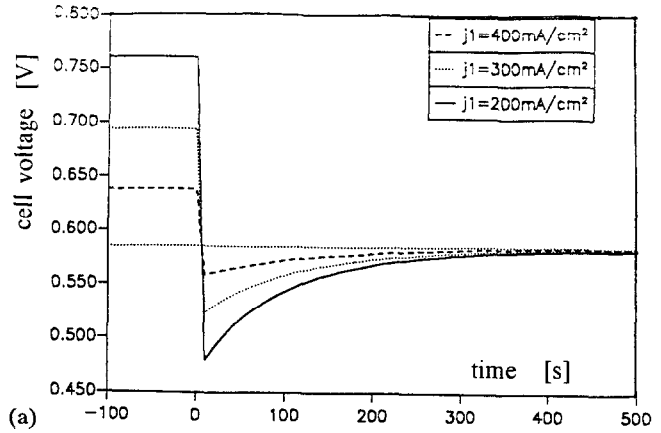

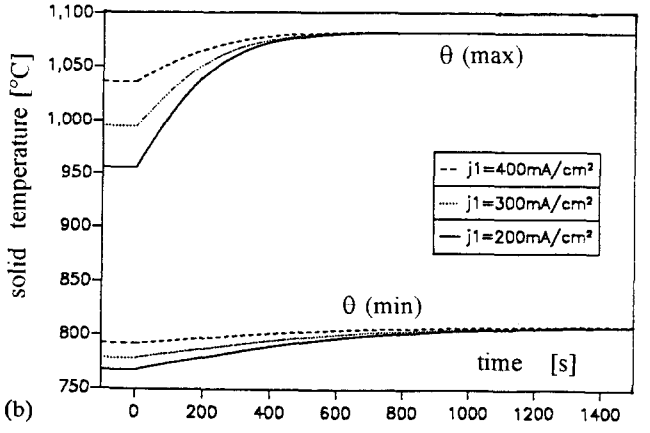

Fig. 8. Effect of load change on (a) cell voltage, and (b) temperature of the cell.

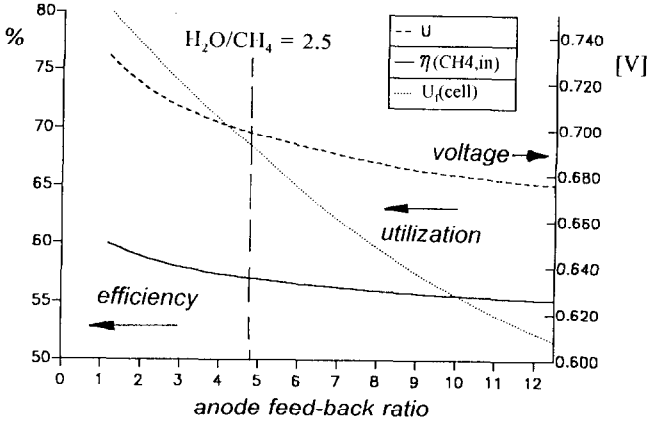

Fig. 9. Effect of feedback ratio on cell voltage, cell efficiency and cell fuel utilization.

their new plateau. The response time of the cell voltage therefore varies with the heat storage capacity of the solid materials.

Recycling of the anode gas

As mentioned above, partial recycling of the anode gas can be applied to utilize the electrochemically produced steam for the reforming reaction. For this the molar stream $\dot{n}_{rec}$ is separated from the anode exhaust gas, fed back and mixed with the oncoming methane $\dot{n}_{CH_4\,in}$. The ratio of both molar streams is the feedback ratio *FR*.

$$FR = \frac{\dot{n}_{rec}}{\dot{n}_{CH_4\,in}} \tag{22}$$

With growing *FR* the anode mass flow through the cell increases which leads to a lower cell fuel utilization and therefore to a more uniform current density distribution. This positive effect is negatively affected by the decrease of the fuel partial pressure caused by the high contribution of the inert gases (H_2O, CO_2). Figure 9 represents some important cell quantities depending on the feedback ratio. In this calculation the total fuel utilization was kept constant at $U_{f(total)} = 85\%$ whereas the cell fuel utilization decreases with increasing *FR*.

The total fuel utilization $U_{f(tot)}$ can be increased under feedback conditions up to $U_{f(tot)} = 95\%$. Thus the minor losses of the cell voltage can be overcompensated in favour of the system efficiency.

Concluding remarks

A mathematical model for the simulation of a planar solid oxide fuel cell has been presented. It accounts for three-dimensional and time-dependent effects. Internal methane-steam reforming and recycling of the anode gas are also considered.

The calculations for a cell with internal reforming yield the following:

- cross-flow cells may be sub-cooled due to the fast reforming reaction
- the highest cell efficiency is reached for counter-flow
- the most uniform current density distribution is observed for co-flow
- the largest temperature gradients in the solid structure occur for cross-flow
- excellent thermal insulation of the stack is necessary to prevent it from cooling-out
- recycling of the anode gas provided to supply the cell with steam also contributes to a higher plant efficiency and more uniform current density distribution
- the response time for load changes is strongly coupled with the solid-temperature; it is in the order of 5 min under the present conditions

The kinetics of the electrochemical and reforming reactions are modelled with relationships which must be considered as preliminary. They will be improved as knowledge in this field increases.

At the present time the computation is based on a uniform mass flow distribution across all channels. This, however, cannot be achieved in a real stack. Therefore a future simulation must take this important fact into account.

Acknowledgement

I would like to thank my colleague Dr Ch. Rechenauer who installed the computer program for his valuable collaboration during this work.

List of symbols

c_p	heat capacity: solid, kJ kg^{-1} K^{-1}; gas, kJ $kmol^{-1}$ K^{-1}
E	activation energy, kJ $kmol^{-1}$ K^{-1}
F	Faraday constant, A s mol^{-1}
FR	feedback ratio
G	Gibbs free enthalpy, kJ mol^{-1}
h	channel height, m
j	current density, mA cm^{-2}
k	pre-exponential factor, according to definition
m	exponent
$\dot{n}$	molar flux, mol s^{-1}
P	electrical power, W
p	partial pressure, N m^{-2}
R	gas constant, kJ $kmol^{-1}$ K^{-1}
R_i	specific electrical resistance, Ω cm^2
s	distance element, m
T	temperature, K
t	time, s
U	voltage, V
U_f	fuel utilization
x, y, z	coordinates, m

Greek symbols

α	heat transfer coefficient, W m^{-2} K^{-1}
ϵ	accuracy threshold
η	efficiency
λ	air ratio
λ_{ef}	effective conductivity, W m^{-1} K^{-1}
λ_h	heat conductivity, W m^{-1} K^{-1}
Φ	source term, W m^{-3}
ρ	density, kg m^{-3}
θ	temperature, °C

Indices

a	air
A	anode
C	cathode
ed	educt
ef	effective
el	electrochemical
f	fuel
h	heat
in	entrance
max	maximum
min	minimum
n	molar
out	outlet
prod	product
tot	total

″ referred to area
′ referred to volume

References

1 C.G. Vayenas and L.L. Hegedus, *Ind. Eng. Chem. Fundam., 24* (1985) 316–324.
2 J.R. Selman, *International Energy Agency, Workshop Mathematical Modelling, Proc. Natural Gas Fuelled Solid Oxide Fuel Cells and Systems, Charmey, Switzerland, 1989,* pp. 31–64.
3 J.R. Selman, M. Flück and R. Gruber, *International Energy Agency, Proc. Workshop Modelling and Evaluation of Advanced SOFC, Hertenstein, Switzerland, June 24–29, 1990,* pp. 17–45.
4 M. Flück and R. Herbin, *International Energy Agency, Workshop Mathematical Modelling, Proc. Natural Gas Fuelled Solid Oxide Fuel Cells and Systems, Charmey, Switzerland, 1989,* pp. 229–240.
5 E. Erdle, J. Groos, H.G. Müller, W.J.C. Müller and R. Sonnenschein, Energy, *Modelling of the Mass and Energy Balances of SOFC Modules, Rep. EUR 13158 EN,* Commission of the European Communities, 1991.
6 S. Ahmed, C. McPheeter and R. Kumar, *J. Electrochem. Soc., 138* (1991) 2712–2718.
7 J.R. Ferguson, *Proc. 2nd Int. Symp. Solid Oxide Fuel Cells, Athens, Greece, 1991,* pp. 305–312.
8 E. Arato and P. Costa, *Proc. 2nd Int. Symp. Solid Oxide Fuel Cells, Athens, Greece, 1991,* pp. 273–280.
9 I.V. Yentekakis, S. Neophytides, S. Seimanidis and C.G. Vayenas, *Proc. 2nd Int. Symp. Solid Oxide Fuel Cells, Athens, Greece, 1991,* pp. 281–288.
10 T. Sira and M. Ostenstad, *Proc. 3rd Int. Symp. Solid Oxide Fuel Cells, Honolulu, HI, USA, May 16–21, 1993,* pp. 851–860.
11 Ch. Bleise, J. Divisek, B. Steffen, U. König and J.W. Schultze, *Proc. 3rd Int. Symp. Solid Oxide Fuel Cells, Honolulu, HI, USA, May 16–21, 1993,* pp. 861–867.
12 J.-M. Fiard and R. Herbin, *Les Publications du L.A.M.A.,* Université de Savoie, May, 1993.
13 A. Malandrino and M. Chindemi, *Proc. 3rd Int. Symp. Solid Oxide Fuel Cells, Honolulu, HI, USA, May 16–21, 1993,* pp. 885–894.
14 H. Karoliussen and K. Nisanciouglu, *Proc. 3rd Int. Symp. Solid Oxide Fuel Cells, Honolulu, HI, USA, May 16–21, 1993,* pp. 868–877.
15 Ch. Rechenauer and E. Achenbach, *Rep. Jül-2752,* Apr. 1993.
16 J. Mizusaki, H. Tagawa, M. Katou, K. Hirano, A. Sawata and K. Tsuneyoshi, *Proc. 2nd Int. Symp. Solid Oxide Fuel Cells, Athens, Greece, 1991,* pp. 487–494.
17 K. Eguchi, T. Inoue, M. Ueda, J. Kaminae and H. Arai, *Proc. 2nd Int. Symp. Solid Fuel Oxide Fuel Cells, Athens, Greece, 1991,* pp. 697–704.
18 F. Umemura, K. Amano and Y. Ochiai, *Proc. 2nd Int. Symp. Solid Oxide Fuel Cells, Athens, Greece, 1991,* pp. 153–158.
19 J.L. Bates, L.A. Chick, G.E. Youngblood and W.J. Weber, *Semi-annual Progress Rep.,* Pacific Northwest Laboratories, Richland, WA, USA, Oct. 1990.
20 K. Tsuneyoshi, M. Mori, A. Sawda, J. Mizusaki and H. Tagawa, *Solid State Ionics, 35* (1989) 263–268.
21 H. Taimatsu, K. Wada and H. Kaneko, *Proc. Int. Fuel Cell Conf., Makuhari, Japan, 1992,* pp. 377–380.
22 K. Wippermann, U. Stimming, H. Jansen and D. Stöver, *Proc. 3rd Int. Symp. Solid Oxide Fuel Cells, Honolulu, HI, USA, May 16–21, 1993,* pp. 180–189.
23 K. Eguchi, T. Setoguchi, M. Sawano, S. Tamura and H. Arai, *Proc. 2nd Int. Symp. Solid Oxide Fuel Cells, Athens, Greece, 1991,* pp. 603–610.
24 J.P.P. Huijsmans, F.H. van Heuveln, J.P. de Jong and D. Bos, *Proc. Int. Fuel Cell Conf., Makuhar, Japan, 1992,* pp. 353–356.